Protonation and structural/chemical stability of Ln2NiO4+δ ceramics vs. H2O/CO2: high temperature / water pressure ageing tests

Settakorn Upasen, Pierre Batocchi, Fabrice Mauvy, Aneta Slodczyk, Philippe Colomban

HAL Id: hal-01083734
https://hal.sorbonne-universite.fr/hal-01083734

Submitted on 18 Nov 2014

Protonation and structural/chemical stability of $Ln_2NiO_{4+\delta}$ ceramics vs. H_2O/CO_2: high temperature / water pressure ageing tests

S. Upasen[a,b], P. Batocchi[c], F. Mauvy[c], A. Slodczyk[a,b], Ph. Colomban[a,b*]

[a] Sorbonne Universités, UPMC Univ Paris 06, UMR 8233, MONARIS, 75005, Paris, France
[b] CNRS, UMR 8233, MONARIS, F-75005, Paris, France
[c] ICMCB, ICMCB-CNRS-IUT-Université de Bordeaux, 33608 PESSAC Cedex, France

corresponding author : philippe.colomban@upmc.fr

ABSTRACT:

Mixed ionic-electronic conductors (MIEC) such as rare-earth nickelates with a general formula $Ln_2NiO_{4+\delta}$ (Ln=La, Pr, Nd) appear as potential cathodes for energy production and storage systems: fuel cells, electrolysers and CO_2 converters. Since a good electrode material should exhibit important stability in operating conditions, the structural and chemical stability of different nickelate-based, well-densified ceramics have been studied using various techniques: TGA, dilatometry, XRD, Raman scattering and IR spectroscopy. Consequently, $La_2NiO_{4+\delta}$ (LNO), $Pr_2NiO_{4+\delta}$ (PNO) and $Nd_2NiO_{4+\delta}$ (NNO) have been exposed during 5 days to high water vapour pressure (40 bar) at intermediate temperature (550°C) in an autoclave device, the used water being almost free or saturated with CO_2. Such protonation process offers an accelerating stability test and allows the choice of the most pertinent composition for industrial applications requiring a selected material with important life-time. In order to understand any eventual change of crystal structure, the ceramics were investigated in as-prepared, pristine state as well as after protonation and deprotonation (due to thermal treatment till 1000°C under dry atmosphere). The results show the presence of traces or second phases originating from undesirable hydroxylation and carbonation, detected in the near-surface layers. The proton/water insertion modifies the structure symmetry and the unit-cell volume whatever the low amount (<0.5 wt% equivalent H_2O). This result is consistent with long range interaction and in contradiction with the formation of hydroxyl species hypothesis. The reaction mechanisms evidenced after autoclave treatment may be useful to understand the reaction occurring at the electrode surface in SOFC/HTSE systems.

KEYWORDS: electrode, chemical stability, proton, water pressure, microstructure, CO_2

Highlights

High temperature/water pressure autoclave is used to study the reaction/corrosion at SOFC/HTSE electrode.

High stability of $Pr_2NiO_{4+\delta}$ (PNO) and $Nd_2NiO_{4+\delta}$ (NNO) dense ceramics vs. water pressure is demonstrated.

Protonated rare-earth nickelates retain the perovskite-type structure and their H-content is determined.

Very low laser illumination power is required to avoid RE nickelate phase transition.

Nickelates show increasing stability from La to Pr/ Nd vs. CO_2-rich high temperature water vapour

1. INTRODUCTION

During the last decades, perovskite-type oxides have been developed as electrolytes and electrodes for Solid Oxide Fuel Cells (SOFC), including Proton Ceramic Fuel Cells (PCFC), gas separation membranes and High Temperature Steam Electrolysers (HTSE)[1-3]. An efficient electrode material should possess high electronic and ionic conductivity (so called MIEC, mixed ionic-electronic conductor), protonic conductivity for instance in the case of air/hydrogen SOFC/HTSE operating at medium to high temperature. The main goal of these technologies is to reduce the operating temperature in the 500 - 700°C range [4-8]. A tolerant behavior vs. CO_2 traces is also requested for these compounds. Furthermore, stable materials vs. CO_2 are searched for the conversion of CO_2 into CH_4 or more valuable chemicals by reaction between carbon dioxide gas and hydrogen produced at the cathode [7]. Recently, perovskite-type ceramics belonging to Ruddlesden-Popper family such as Rare-Earth (RE) nickelates with a general formula $Ln_2NiO_{4+\delta}$ (Ln = La, called here after LNO; Pr (PNO) and Nd (NNO)) are proposed as potential FC cathodes [8-12].

The ideal perovskite structure has a cubic symmetry with the $Pm\bar{3}m$ space group [6]. No Raman peaks are expected for such cubic symmetry and thus the Raman spectroscopy is very efficient to detect any structural distortion [13]. The symmetry of $Ln_2NiO_{4+\delta}$ is more or less distorted either tetragonal (P42/ncm), or orthorhombic Bmab or Fmmm, depending on the lanthanide elements, the oxygen stoichiometry δ and temperature [14-21]. Phase coexistence is also often reported in polycrystalline materials. As for most of perovskites, the structural phase transitions are observed with the temperature increase, for example in the case of NNO with an oxygen excess, the transition from the orthorhombic symmetry *(Fmmm)* to the tetragonal (*I4/mmm*) one is detected between 477/550°C and 600/627°C depending on authors [14-21], actually depending on the oxygen partial pressure explored during the thermal treatment. This should be stressed, the black color of a material requires special procedure for optical studies in order to avoid any local heating and associated structural changes (oxidation/stoichiometry modification) [22,23].

In this study, the chemical/structural stability of well-densified LNO, PNO and NNO ceramics exposed to high water vapor pressure (40 bar), with or without the CO_2 gas dissolved in the water, at 550°C during 5 days using the autoclave device have been compared [24]. The high water pressure increases water activity at a ceramic surface and hence enhances reaction (hydroxylation, carbonation, protonation) degrees. Consequently, a significant amount of secondary phases can be formed due to corrosion process. It can be noticed that accelerate and large formation of such undesirable phases makes their detection and characterization easier. Thermogravimetry (TGA), thermal expansion (TE), infrared spectroscopy (IR), Raman spectroscopy (RS) and X-ray diffraction (XRD) were employed in order to identify potential corrosion mechanisms as well as structure modifications involved and/or associated to proton/water reaction/insertion. The combination of the microstructure examination with Raman mapping was used in order to establish the reaction rates. Preliminary conclusions have been reported [25].

Finally we claim to deal also with the complex behaviour of proton in the case of anhydrous proton conducting oxides. It should be stressed that the fundamental knowledge on the proton chemical nature (hydroxyl groups or interstitial protons), its exact content, its localization (differentiation between surface defects and bulk species), and the dynamic of protons remain poor and highly debated [26-30]. The unique properties of proton and its low amount (i.e. a doping) in these membranes yield the study difficult.

Consequently many authors do not even try to determine the H content in their studied/used materials. The comprehension of the structural modification involved by protonation is required for the understanding of the MIEC electrode ageing.

2. EXPERIMENTAL

Synthesis and sintering: Commercial powders provided by the Marion Technologies company (Verniolle, France) were isostatically pressed into pellets at 3000 bars for 5 min and then sintered in air at 1350 °C for 4 hours. Densities of the as-prepared ceramics measured by the Archimedes method were higher than 95 % of the theoretical values.

Autoclave treatment: Protonation was performed at high temperature/high water vapour pressure using autoclave device (Top Industrie, Vaux le Pénil, France)[14-17]. The ceramics were placed on the gold-foil holder, and then put in the autoclave chamber. Two kinds of water were used: the decarbonated water from ultrapure water system immerged by N_2 gas for 20 minutes in order to eliminate CO_2 amount (the so-called lean-CO_2 water), and another one, the room temperature CO_2 saturated water (hereafter called rich-CO_2 water).The dwell water pressure is adjusted by controlling the maximal pressure. A ~10 to 20 % decrease of the pressure is observed during the dwell duration (550°C, 5 days), that indicates consumption of water by the ceramic pellets.

Thermogravimetry analysis: TGA of both as-prepared and protonated ceramic pellets was performed using a Setaram Setsys Evolution (Setaram, Caluire, France) instrument in the 25°C – 1000°C temperature range (heating rate of 5°C/min). In order to enhance the accuracy of TG measurements in the studied temperature range, a Pt crucible and Helium atmosphere (99.99%, H_2O < 3 ppm vol., O_2 < 2 ppm vol., C_nH_m < 0.5 ppm vol., Alphagaz-1, Air Liquide, France) were employed. Non-radiative heat transfer is increased in He gas that promotes the instrument sensitivity. Note, the carbon heating resistor guaranties the conservation of low oxygen level.

Thermal Expansion: TE measurements were carried out under argon atmosphere (99.99%, H_2O < 0.5 ppm vol., O_2 < 0.1 ppm vol., CO < 0.1 ppm vol., CO_2 < 0.1 ppm vol., H_2 < 0.1 ppm vol., C_nH_m < 0.5 ppm vol. Alphagaz-2, Air Liquide, France) using a Setaram Setsys 1650 dilatometer instrument equipped with amorphous silica rod and support. Very low thermal expansion of amorphous silica makes a direct comparison of as-measured data possible. Flat pieces of non-protonated and protonated ceramics were measured in 30 – 500°C temperature range for three successive heating/cooling cycles with heating rate of 10°C/min.

Microstructure: The surface and the fresh fracture sections of each sample, in different states, were analyzed in micro-scale, 50-1000µm range, using optical Microscope Olympus instrument with the selected, x10, x50 and x100 objectives. The density of cracks was measured using the cracking-line intercept method (ASTM E112) using x10 objective. The 13 line-bundles were used as intercepting pattern. The distances in between two cracks were measured and the mean value determined.

Raman microspectrometry: Raman scattering spectra were recorded at room temperature using different exciting laser lines and instruments: i) the 458nm line delivered by Kr^+ ion laser; this blue laser line allows avoiding the superimposition of the Raman signature with electronic transitions of 4f ions. Labram HR800 Raman micro-spectrometer (Horiba Jobin Yvon SAS, Longjumeau, France) equipped with a 50x and x10 long working distance Nikon objectives was used; ii) the 785nm solid state source line of a Senterra

3

spectrometer (Bruker Optics, Karlsruhe, Germany) equipped with x10 and x50 long work distance objectives; iii) the 633nm line of a He-Ne laser using a Labram Infinity spectrometer (Dilor, Lille, France). Different spectra were recorded under different illumination powers per surface unit up to the reaching a constant wavenumber indicating that the black material is not perturbed by the laser beam.

Infrared spectroscopy: FT-IR Equinox 55 Irscope microspectrometer (Brucker) was used to record the room temperature infrared spectra between $600cm^{-1}$ and $4000cm^{-1}$ in an ATR mode using the Diamond ATR (analyzed area ~2x2mm^2) or the Germanium micro ATR (noted hereafter µ, analyzed area 20x20 µm^2).

X-ray Diffraction: XRD patterns of ground pellets were collected on a PANalitycal X'pert MPD-PRO Bragg-Brentano θ-2θ geometry diffractometer equipped with a germanium primary monochromator over an angular range of 2θ = 10-130°. Each acquisition lasted for 64 hours. The Cu-Kα$_1$ (λ = 1.54056 Å) radiation was generated at 45 KV and 40 mA. Unit-cell parameters have been calculated by Le Bail profile matching. The relative quantities of the different phases have been determined according to the ratio of the relative intensities of the major peaks recorded on the XRD patterns.

3. RESULTS AND DISCUSSION

3.1. Mechanical stability

Compared to other ceramics exposed to high water pressure in similar conditions [24], the investigated LnNO pellets were not crumbled or strongly cracked after 5 days of treatment and retained significant mechanical strength. Optical microscope observations (Fig. 1) do not show cracks at the micron scale but reveal the presence of white scares (using lean-CO_2 water) or significant deposits (CO_2-saturated water). The black color of the ceramics promotes their detection. Large magnification images show two types of surface deposits: rather well-shaped micron-like grains and larger ~50 µm wide flower-like aggregates. On the contrary, after thermal treatment at 1000°C under dry He atmosphere, the de-protonated PNO and NNO pellets exhibit more or less important crack networks (Fig. 1, mean distance in between cracks is equal to ~200 and 100µm for PNO and NNO, respectively), not observed in the case of thermally treated non-protonated samples. This should be consistent with a variation of the LnNO unit-cell volume observed after the autoclave treatment (see further). Crack formation after thermal treatment can be assigned to a decrease of the unit-cell volume, due to the departure of volatile species (H_2O) with the temperature increase.

3.2. Chemical and Structural modifications

Fig. 2a compares the TGA curves recorded under Helium flux for small pellet pieces of non-protonated and protonated LnNO ceramics. The weight mass loss observed above 500°C for non-protonated pellets is assigned to the modification of the oxygen stoichiometry, according to the mobility of oxygen ions at intermediate temperature [31]. In order to whip out this contribution, the relative difference in weight loss measured between a pristine ceramic and a protonated one is plotted in Fig. 2b. The subtraction of the thermal behavior of pristine materials heated in the same conditions highlights the contribution due to the autoclave treatment. The mass difference between non- and protonated LnNO pellets is low, but three TG events can be clearly observed for LNO and PNO ceramics: a well-defined down step at ~300°C, a smaller one at 500-650°C and a large one at ~900°C. The NNO behavior does not show any marked TG feature.

4

The comparison with series of TGA measurements characteristic of materials containing protonic species [21,24,26,32] led us to assign the first well-defined step to hydroxide(s) decomposition (typically occurring at ~300-400°C), the second one may correspond to the departure of bulk protons and the highest temperature one to the carbonate decomposition (~900°C). According to the TG data the following formula can be proposed for the whole ceramic pellet with the hypothesis that the ceramic is a single phase and that events below 900°C can be assigned to water molecule departure due to OH^- and proton loss while CO_2 departure appears above 900°C: $La_2NiO_{4+\delta}H_{0.77}(OH)_{0.1}(CO_3)_{0.02}$, $Pr_2NiO_{4+\delta}H_{0.53}(OH)_{0.04}(CO_3)_{0.03}$ and $Nd_2NiO_{4+\delta}H_{0.21}$.

Thermal expansion plot (Fig. 2c) shows a contraction jump at ~320°C during the first heating cycle for both protonated LNO and PNO ceramics (not observed in the literature, see [25]). A very small jump is detected in the NNO expansion curve. The contraction jump may explain the crack network observed at the sample surface after thermal treatment of protonated ceramics (Fig 1). A smaller down jump is also observed at ~200°C for all samples; it can be attributed to the contribution of the amorphous silica road that contains some cristobalite and trydimite traces. The very small feature detected at ~450°C could be the signature of previously reported orthorhombic/tetragonal phase transition [3,12,14-16].

The XRD patterns recorded for LNO, NNO and PNO ground pellets before and after autoclave treatment are reported in Fig.3. Concerning the initial state, all compounds are well crystallised and show a single phase [12,17]. Corresponding unit-cell parameters and space group symmetry (orthorhombic Fmmm or Bmab) are given in Table 1.

After protonation extra Bragg peaks are clearly visible and can be assigned to the second phases observed at the sample surface by optical microscopy (Fig. 1). Furthermore, a small shift of peaks is observed indicating a change of the unit-cell parameters (see further). For protonated LNO (H-LNO) and NNO (H-NNO) a coexistence of two perovskite phases is evidenced from the Le Bail profile analysis (Table 1).

Analysis of XRD patterns allowed the identification of three types of secondary phases: hydroxides, carbonates and oxides. Their relative ratios in the case of different Lanthanides cations are listed in Table 2. The significant proportion of hydroxides phases detected for PNO can be related to the well-defined 300°C TG event (Fig. 2 a&b) and the presence of large white surface features (Fig. 1). Regarding the LNO compound, the $La(OH)_3$ amount seems to be lower (see Table 2). This could be explained by the reduced mass variation observed in TGA curves. The identification of Ln-oxohydroxide in the case of NNO ceramic is also consistent with the small thermal expansion jump. The high ratio of carbonates observed for LNO sample is in good agreement with the Raman scattering and ATR-FTIR data (see further).

3.3. Characterisation of the protonated perovskite

The comparison of the symmetry and the unit-cell parameters determined from XRD powder pattern shows complex structure modifications caused by the autoclave treatment. Notwithstanding the formation of surface secondary compounds, the coexistence of two structural phases can be deduced from Le Bail XRD profile matching analysis. The first phase keeps the pristine orthorhombic symmetry Fmmm (D_{2h} point symmetry) (H-LNO) or Bmab/D_{2h} (H-NNO) and the associated unit-cell variations are very low (Table 1). The second one exhibits the tetragonal I4/mmm/D_{4h} (H-LNO & H-NNO) symmetry and rather significant changes of the unit-cell parameters and volume are observed. The unit-cell volume changes are consistent with the

insertion of protonic species into the lattice. Previous studies on the protonation of perovskite pointed out that the proton/water insertion decreases the unit-cell distortions [32,33]

The largest volume variation is measured for LNO whereas the smallest one for PNO. A small volume increase is observed for NNO (+ 2.5% (Bmab) and + 0.2% (I4/mmm). The very low TG weight loss (Fig. 1) indicates that protonation, if occurs, is very low and/or compensated by oxygen stoichiometry variation. On the contrary, a contraction is measured in the case of PNO (2.3%) and LNO (0.2 and 9.3%, for Fmmm and I4/mmm, respectively (Table 1)). It should be noticed that the comparison has been made for different symmetries: thus the I4/mmm unit-cell volume was multiplied by a 2 factor (LNO: 171.86x2 = 343.73 to be compared with 378.85 $Å^3$; NNO: 181.98 x 2 = 363.96 to be compared with 363.10 $Å^3$). For both later compounds the TGA curves are consistent with a protonation.

3.4. Raman signature of pristine nickelates

The collection of Raman spectra of black materials is a difficult task because of the very strong light absorption that induces direct conversion of the photon energy into heat and hence promotes local heating and structural transformations. In consequence, even under low irradiance phase transitions and/or oxidation can be induced by the laser spot [23,23]. Since the degree of light absorption strongly varies with the wavelength, the Raman spectra have been recorded with blue (458 nm) and red (785/633 nm) laser excitation lines. Furthermore Rare Earth elements being largely present in the studied compositions, a superimposition of the (huge) 4f electronic transition fluorescence peaks with the Raman signal is currently observed; consequently a comparison of the Raman signal recorded with different wavelengths is necessary to select the most appropriate laser excitation [25]. Under 458nm and 785 laser excitations broad bands and multiplets due to 4f electronic transition are observed above ~1200 cm^{-1} (i.e. 866.7 nm in absolute scale,) and thus do not overlap with the Raman spectrum. Consequently only spectra recorded under blue excitation are presented in Fig. 4 because of their better quality (see ref. [25] for spectra recorded under different laser wavelength).

The Raman signature of non-protonated, pristine ceramics will be first discussed. Most of Raman spectra reported in the literature is of poor quality and deals with homologues [34-40]. Ogita *et al.* [34] analyzed the Raman spectra of Rb_2NiO_4 single crystal with the K_2NiF_4-type structure as well as polycrystalline La_2NiO_4 (514.5 nm, output power of about 300mW). In the case of tetragonal I4/mmm (D_{4h}^{17}) symmetry 14 optic modes are expected ($2E_g+2A_{1g}+5E_u+4A_{2u}+B_{2u}$), 4 ($2E_g+2A_{1g}$) being Raman active, and 7 ($4E_u+3A_{2u}$) infrared active. Nevertheless, it is well established that the symmetry depends on the oxygen stoichiometry which can be modified by sintering and laser heating [37,38]. Ogita et al. assign the Raman peaks detected at 120 cm^{-1} and 358 cm^{-1} to A_{1g} modes associated to the motion of the heavy Rb cations (see Fig.5). The peak at 188 cm^{-1} was assigned to the E_g mode. Comparing the spectra of polycrystalline La_2NiO_4 with those of Rb_2NiO_4 single crystal, the authors assigned the peaks at 100 and 405-430 cm^{-1} (according to the analyzed spot) to A_{1g} modes. The above reported Raman signatures can be questioned, in particular the 100-120 cm^{-1} peak because these bands are observed for rare-earth oxides and (oxo)hydroxides (Table 4). Udagawa *et al.* [35] studied polycrystalline $(La_{1-x}Sr_x)_2NiO_4$ (488 nm, output power of 20mW). Two Raman modes were observed at 450 cm^{-1} and 240 cm^{-1}, assigned to the Ni-O stretching (A_{1g}) and apical oxygen vibration along the a- or b-axis with E_g symmetry, respectively. Prieto *et al.* [36] studied the stoichiometric and oxidized Nd_2NiO_4 polycrystalline samples (488 nm, 3W power). The 440-470 cm^{-1} band is assigned to the Ni-O(2) stretching modes and the features from 750 to 1000 cm^{-1} to the double phonon of the first mentioned modes because

6

of resonance Raman condition [37,38]. The authors observed the Ni-O stretching mode at 670 cm^{-1}. Because, this mode is forbidden in the tetragonal *I4/mmm* symmetry, some distortion of the unit-cell can be supposed.

The discrepancy between literature data and the black color of the ceramic led us to study the wavenumber shift versus laser power. Fig. 5 compares the wavenumber shift vs. logarithmic laser power for different samples. Below ~0.3 mW (x50 objective) the wavenumber is nearly constant that proves the absence of heating phenomena. As expected [23], a linear wavenumber down shift of the main peaks (Fig. 5) is observed vs. logarithmic laser power for values higher than 0.3 mW, in agreement with the sample heating. In between these two regimes, an up wavenumber jump is observed. This behavior can be assigned to a phase transition/oxydation due to the laser heating in air. Consequently, only Raman data recorded with a low illumination power can be used for comparison with XRD data.

The Raman spectra collected at low illumination power for all pristine LnNO samples (Fig. 4) show triplet located at ~ 220, 450-470 and 650-675 cm^{-1}; a weak, broad band can also be detected at 590 cm^{-1}. Similar spectra have been recorded at the surface and on fresh section of pristine ceramic pellet. Note, narrow peaks almost disappear under red laser excitation [25] – the spectrum becomes characteristic of low distorted cubic perovskite structure – that could indicate a resonance spectrum under blue laser excitation. The LNO spectrum is very similar to that of other perovskite compounds, like orthorhombic LaMnO$_{3-\delta}$ [39] and SrFe$_{1-x}$Ga$_x$O$_{3-\delta}$ [40]. Note, sometime observed very narrow ca. ~860 cm^{-1} peak is due to CrO$_4^{2-}$ ions pollution arising from the autoclave steel. When the oxygen stoichiometry and the symmetry are modified, a band broadening and an intensity decrease/disappearance of the ~660-700 cm^{-1} peak for LNO and NNO can be observed as for above mentioned homologues perovskite [39,40]. However, the wavenumber up-shift measured for LNO and NNO compounds, cannot be explained by the heating (thermal expansion of the chemical bond led to a down-shift) but indicates a phase transition. The wavenumber and the intensity of the peaks slightly vary from spot to spot and it is not possible to definitely conclude if this small wavenumber shift arises from the local variation of the stoichiometry, grain orientation, stress, etc. At higher laser power irradiance, the wavenumber down-shift can be assigned to thermal lengthening of the M-O bond under the laser spot, as usual. It could be added that in the case of all LnNO thermally treated samples (1000°C under He atmosphere), the peak at ca. 655 (NNO) to ~680 cm^{-1} (LNO) becomes very significant. This contribution can be assigned to the distortion increase, as previously noted by Prieto et al. for NNO [36], likely to D$_{2h}$. or even lower symmetry. Simultaneously a broad feature is observed at ~1350 cm^{-1} that may be the overtone of the mentioned above, 670 cm^{-1} band according to the resonance Raman effect under blue excitation. The comparison of the spectra (relative band intensity, bandwidth, splitting) clearly demonstrates that the symmetry is slightly different between LNO and the PNO/NNO homologues and changes with temperature. Actually the most important information obtained from the Raman spectrum for perovskite compounds is not only the band number (to be compared with expected number deduced from Group theory analysis), but the Raman intensity that measures the deviation from a cubic mean symmetry [13,23]. The low intensity and important broadness of the PNO and NNO spectra are rather similar to those recorded for rhombohedral Lanthanum Strontium Cobalt Ferrite [25] and rhomboedral perovskite homologues [39,40]. On the contrary, the LNO spectrum is consistent with an orthorhombic symmetry, in agreement with X-ray diffraction (Table 1).

3.5. Reactivity and second phases: hydroxylation and carbonation

Autoclave treatment involves structural changes and corrosion phenomena. Figure 4 presents typical Raman spectra recorded on the surface and section of the LnNO protonated ceramics. The Raman mapping recorded along a fresh fractured section of autoclave treated ceramics is presented in Fig. 6. An important number of recorded Raman spectra allow detecting the presence of different layers (Fig. 7) and determining their thicknesses. Note, significant FTIR-ATR spectra are shown in Figs 8 & 9. Starting from the surface, 3 characteristic regions can be distinguished: the corroded layer, the 'high' protonated layer and the 'low' or non-protonated core.

A mixture of hydroxide(s), carbonate(s) or hydroxycarbonate(s), can be identified by the presence of narrow peaks, fingerprints of these phases (Table 3, [30,41-46], in agreement with X-ray diffraction, Table 2). Carbonates are well identified due to the C-O narrow Raman stretching mode, centred at 1086 cm^{-1} for La, and at 1084 cm^{-1} for Nd-based carbonate. Note, the narrow IR bending mode peaking at 853 (LNO, Fig. 8a&a', spectrum noted P_s) and 884 cm^{-1} (PNO, Fig. 8b, spectrum noted P_s1) is characteristic of carbonate [46]. Note, ATR FTIR spectra show unexpected reflection spectra, see further). The carbonate contributions seem to be weaker or disappear for materials treated with the CO_2-lean water (see in ref [25]). According to XRD, no carbonates are detected on PNO and NNO surfaces when water with low CO_2 content is used. On the other hand, carbonates are observed for all materials exposed to the CO_2-saturated water vapour pressure.

The Raman spectra of protonated LNO pellet surface (Figs 4a and 6) show additional peaks at 396, 263, 197 and 79 cm^{-1}. These peaks can be assigned to the hexagonal phase of $La_2O_2CO_3$, in agreement with the XRD data. It can be noticed that the small and constant wavenumber shift by comparison with literature data (Table 3) arises from instrument calibration and different laser power.

The spectrum of protonated PNO (Figs 4b & 6b) shows a strong peak at 149 cm^{-1} and an additional small one at 277 cm^{-1}; these peaks are very similar to those characteristic of $La(OH)_3$ and LaOOH (Table 3; the spectra of $Pr(OH)_3$ and PrOOH have not been identified in the literature). Careful examination of the protonated LNO Raman spectra also shows a small ~150 cm^{-1} peak attributed to traces of LaOOH/$La(OH)_3$. Most of these phases can also be identified by the IR spectroscopy (see further IR spectra in Fig. 8). The detection of a 122-135 cm^{-1} doublet in Raman spectrum of protonated NNO (Figs 4c & 6c) and of the 3600 cm^{-1} narrow peak in IR spectrum (not shown) indicates the formation of NdOOH in agreement with XRD data (Table 1). The 335 cm^{-1} peak reveals a formation of Nd_2O_3. There is thus a very good agreement between XRD and vibrational analysis in the identification of formed second phases. Although the resonance character of the NiO Raman spectrum, the broadness of the bands makes its detection difficult. The broad feature centred at ~1100 cm^{-1} observed in LNO (Fig. 4a) and NNO (Fig. 4c) spectra could be the signature of NiO traces.

ATR-FTIR technique specifically probes the sample surface, typically a few (tenths) micron in-depth penetration: the exact penetration depth varies with the wavenumber depending on the optical index of the crystal probe (diamond or germanium; spectra collected with the small Ge crystal are noted µs, Fig. 8) and the sample [47]. Depending on the band intensity and optical characteristics of the studied solid, the band shape is complex and can be described as a mixture of absorption and reflection signal [47,48].

8

Measurements made on the non-protonated (T) and de-protonated (DP) samples (Fig. 8) show the absorption spectra characteristic of traces of protonic species adsorbed at the ceramic surface: broad O-H stretching and bending at 3400 and 1650 cm^{-1}. On the other hand, the ATR-FTIR spectra recorded for protonated ceramics (Fig. 8) exhibit derivative-like signal characteristic of reflection phenomenon: very narrow for low intensity symmetric (at ~745 and 850 cm^{-1}) and broad in the case of intense asymmetric CO_3 bands (~1460 cm^{-1}, Fig. 8a'). Such detection of the strong reflexion spectrum instead of (or superimposed to) the absorption IR spectrum indicates a strong increase of the optical index of the ceramic, according to the increase of its metallic character, a modification related to the stoichimetry change and/or proton insertion. The intensity increase observed for ceramic treated with CO_2 saturated water is assigned to a larger amount of formed carbonates.

3.6. The 'protonated' nickelates

Raman spectrum of the core of the protonated ceramic pellet (3rd layer) is rather similar to that of the pristine material (Fig. 6). This suggests that the ceramic bulk is not protonated or the protonation level is too small to give significant change. On the contrary, large modifications are observed for the intermediate phase between the ceramic bulk and the corroded layer. (Figs 4 & 6):

- For LNO: the ca. 440 cm^{-1} mode splits into two peaks (415-455 cm^{-1}). Two new peaks are also detected: a~160 cm^{-1} one appears and a ca. 610 cm^{-1} peak is observed in place of the 678 cm^{-1} one.
- For protonated PNO and NNO the broadening of bands is observed and the splitting is less visible. As for LNO a band downshift and new peaks are observed at ~140 cm^{-1}.

After thermal treatment (deprotonation), the spectra of all LnNO ceramic become rather similar, with small wavenumber downshift for NNO (Figs 4 & 8, Table 3). This indicates that the changes induced by the deprotonation are rather similar and the pristine structure is (almost) recovered.

Complementary measurements are necessary to establish if the observation of two different structures arises from the incomplete protonation of the pellet bulk or from the existence of two structures with different H content. The first assumption seems to be more relevant. With the later hypothesis, the small unit-cell variation (Table I) could be due to modifications of the oxygen stoichiometry during the autoclave treatment.

The differences between pristine and thermally treated ceramics as well as between thermally treated and de-protonated ones, detected by Raman scattering are confirmed by the results of ATR-FTIR: the main IR band of the perovskite structure is well detected in the case of non-protonated samples at ~700-730 cm^{-1}; this band disappears for protonated ceramics (Fig. 8) according to the change caused by the protonation. The ATR-FTIR spectrum is dominated by the reflection spectrum of the corroded layer. Magnification of the Raman high wavenumber range allows detecting the O-H stretching components of hydro- and oxyhydroxides (Fig. 9 b' & d'). Protonation is however confirmed by comparing the spectra recorded before protonation and after thermal treatment of the protonated ceramic. A significant wavenumber shift between pristine and thermally treated (non-protonated) material (e.g; 694 To 699 cm^{-1} for LNO, 689 to 717 cm^{-1} for PNO) is observed. This indicates an irreversible modification of the pristine structure after the protonation-deprotonation process.

3.7. Chemical stability

As previously mentioned, the examination of the ceramic cross section from the up -surface to down-one shows more details, in particular when action of CO_2-lean and CO_2-saturated water are compared. Raman spectra recorded according to the so-called profilometry method [33] on previously protonated pellet section fracture are reported in Fig. 6; the measurement steps vary from a few microns close to the surface to 50 µm in the section center. The thickness of the different layers formed by the thermal treatment in the autoclave is given in Table 5.

The modification of the upper and lower layers is obvious for LNO (lean- and rich-CO_2 saturated water) and for PNO (rich-CO_2 saturated water only). The use of rich-CO_2 saturated water gives rise to the carbonate formation up to ~10 µm depth after 5 days of treatment at 550°C/40bar. The structure of the upper layers in between the modified surface and the ceramic bulk is different.

The detrimental effect of CO_2 is clear (Table 5). The easiest carbonation of LNO ceramic seems to be obvious. An asymmetry of the corrosion is observed (Fig. 6). This phenomenon could be related to the sample holder design: one of the surface areas is well exposed to the vapor pressure whereas the other is in direct contact with the gold support.

The number of secondary phase detected by Raman analysis is higher than that observed by XRD. In the Raman technique, the combination of the black color of the pristine material/substrate and of the laser spot can lead to uncontrolled transformations (partial dehydration) under the laser light. The dehydration of hydrated/hydroxylated Ln derivatives may induce the formation of series of phases that explains the higher number of vibration modes detected by spectroscopy [30]. On the other hand, vibrationnal spectroscopy is able to reveal the presence of amorphous oxohydroxides not detectable by XRD.[22,30]

Considering materials exposed to CO_2-rich water, the Raman spectrum recorded in the bulk of the pellets can be considered as characteristic of the pure pristine perovskite. On the other hand the material located in between the later core and the corroded layer is the protonated phase. The spectrum with strong 93 cm^{-1} narrow peak can be assigned to lanthanum oxide La_2O_3 (Fig. 9 a & b). This result reveals that the pronotation is not complete and the H content measured by TGA for the whole pellet is lower than the value intrinsically present in the intermediate protonated layer. Taking into account that the volume ratio of the effectively protonated layer retaining the perovskite structure is about 1/3 of the total volume of the LNO and NNO pellets and less than 1/6 of that of PNO ceramic, the following formula could be proposed for the protonated perovskite: $La_2NiO_{4+\delta}H_2$, $Pr_2NiO_{4+\delta}H_4$ and $Nd_2NiO_{4+\delta}H_{0.5}$.

The down shift of the ca. 420-440 cm^{-1} main peak and the unit cell volume variation seem to be consistent with the protonation. These modifications can also be correlated with the lengthening of Metal-Oxygen bond(s) because of the interaction between some oxygen atoms and interstitial or more or less bounded protons. Actually the nature of the 'inserted' proton is not known, the water insertion equation being

$$H_2O + LNO => LNO [H^+]_x [OH^-]_y (x + y = 2)$$
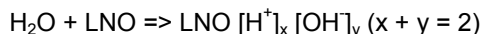
Considering the high wavenumber range (Fig. 9 b' & d'), at least two different hydroxylated compounds are formed, with characteristic ν_{OH} bands at ~3500 and 3570 cm^{-1}. The narrowness of the later band is consistent with the presence of $Ln(OH)_3$ compound, although no reference data have been found in the literature. The unexpected strong reflexion IR signature of the corrosion film is consistent with a strong modification of the perovskite optical index anticipating an increase of the electronic conduction of H-LNO perovskites.

4. Conclusion

Raman, IR, XRD and TGA studies performed on three LnNO dense ceramics exposed 5 days to high water vapor pressure at 550°C, i.e. the temperature designed for SOFC and HTSE systems, reveal that these compounds show rather good stability vs. high water pressure until 40 bar. Note, this is a pressure value 2 to 5 times higher than that required in an industrial use [7]; one can then suppose that the rate of ageing process at lower water pressure should be much lower. Obviously, surface carbonation is increased by using the CO_2 saturated water. $Nd_2NiO_{4+\delta}$ (NNO) ceramic exhibits the highest structural, mechanical and chemical stability. $Pr_2NiO_{4+\delta}$ (PNO) shows the most important content of bulk protons, although it's significant surface hydroxylation. XRD, IR and Raman scattering results allowed to identify the corrosion layer,phases, as (oxo)hydroxides and carbonates. Unit-cell volume contractions are observed in the case of PNO and LNO compounds, the largest one being measured for LNO whereas the smallest is detected for PNO. On the contrary, a small unit-cell volume expansion is observed for NNO but the low TGA mass loss indicates that most of the modifications is rather related to the oxygen stoichiometry change in the used He atmosphere, the protonated layer being rather limited. The local heating under the laser spot induces phase transformation/transition and can lead to data misinterpretations. The use of very low laser power illumination shows similar Raman signature for all protonated perovskite, with a significant downshift of the peak wavenumber, according to modifications of the structure. The peculiar ATR-FTIR spectra recorded on protonated ceramics suggest a modification of the electronic band structure according to the proton insertion, as already detected in the case of Tungsten bronzes [26]. As observed for earth-alkaline proton conducting perovskites [24,30], surface hydroxylation and carbonation competes with water/proton insertion. The reactions taking place in autoclave should also be present at the SOFC/HTSE electrode surface. At the working temperature range hydroxides are good proton conductors [26] and their presence is not detrimental if the formation rate is sufficiently low and if it does not lead to crack formation.

FIGURES CAPTIONS

Fig. 1: Optical microphotographs of the surface of protonated LNO (P-LNO) and PNO (P-PNO) ceramics at different magnification. Comparison is given with de-protonated PNO sample (dP-PNO).

Fig. 2 Representative weight loss of (a) pristine or protonated (p) NNO, LNO and PNO ceramics and corresponding weight loss differences (b) ; the thermal expansion curves measured on a protonated LNO and NNO ceramics (3 heating-cooling cycles) are given in (c)

Fig. 3: Comparison of the XRD patterns before and after protonation of LNO, NNO and PNO crushed ceramics. Protonation has been made used lean-CO_2 water.

Fig. 4: Representative Raman spectra (a) recorded with blue (458nm) laser line of pristine, protonated (P: 40 bar, 7days and 55 bar, 8 days), de-protonated (DP) and thermally treated (T). The laser power at sample is given; x50 microscope objective is used. In (b) spectra recorded at low and very low laser power are given. The pellet is polished (P) in order to record representative spectra of the different layers.

Fig. 5 Semi-logarithmic plot of the wavenumber vs laser power (0.01 to 30 mW, 488nm, x50 objective) for LNO, PNO and NNO.)

Fig. 6: Raman profilometry along the fresh section fracture of LNO and PNO ceramic pellets protonated using lean-CO_2 and rich-CO_2 water. The use of low magnification microscope objective (e.g. x10) lowers the illumination power /surface unit and avoids phase modification under the laser spot.

Fig. 7 Comparison of the thickness of the different layers formed after autoclave treatment in CO_2-lean (L) and -rich (H) water for 5 day at °C, 40 bar H_2O.
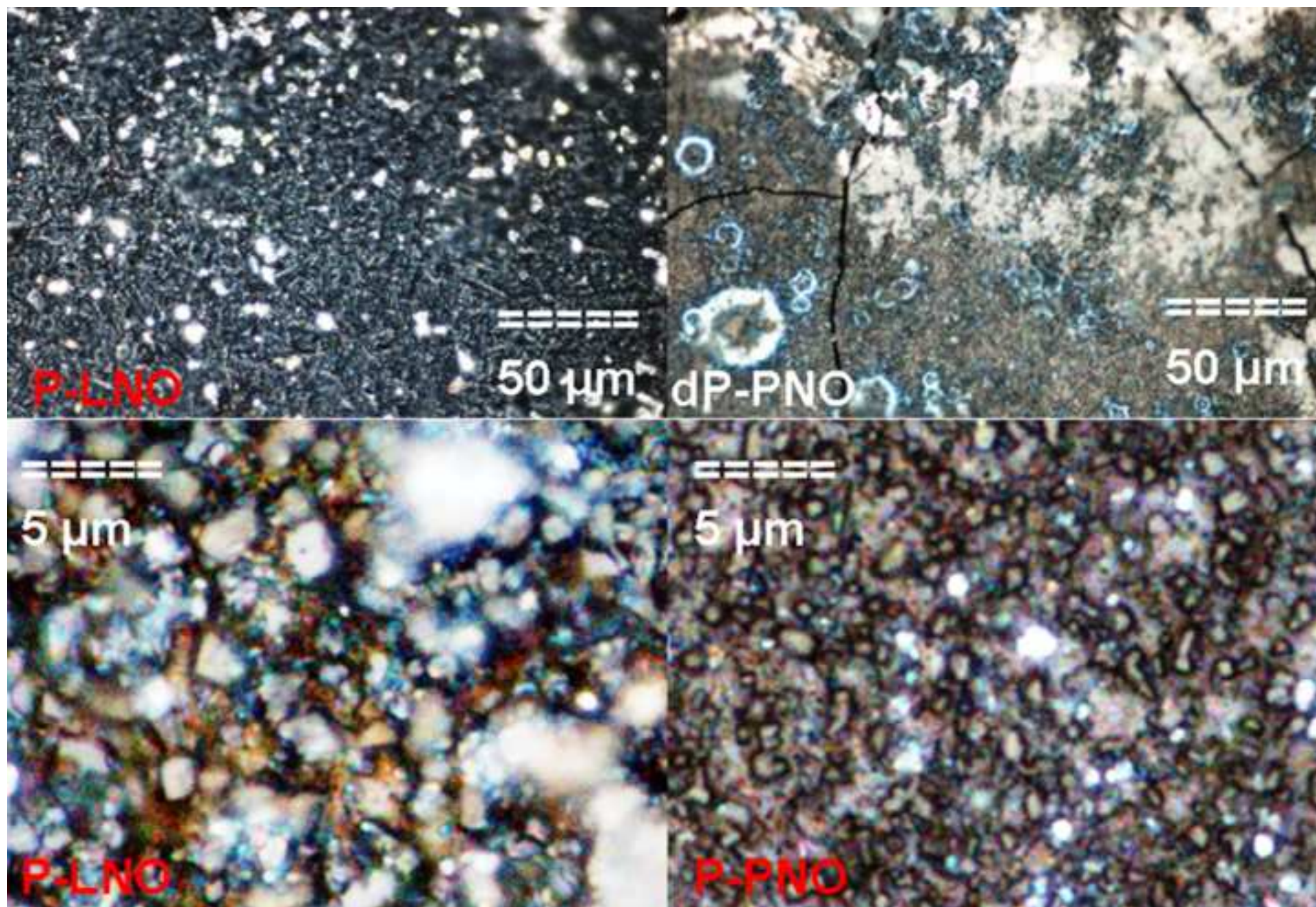
Fig. 8: ATR and microATR-FTIR (µ) spectra recorded at the surface of protonated (P), de-protonated (DP) and thermally treated (T) LNO and PNO ceramics. Comparison is made with protonated LNO ceramic using CO_2 saturated water. The in-depth probed surface layer varies when Germanium (µ ATR FTIR) or Diamond (ATR FTIR) are used.

Fig. 9: Detail of the Raman profilometry along the fresh section fracture of LNO and PNO ceramic pellets protonated using lean-CO_2 and rich-CO_2 water

References

1. T. Ishihara, Perovskite Oxide for Solid Oxide Fuel Cells. Springer, Dordrecht Heidelberg London New York, 2009.
2. S.J. Skinner, Characterisation of $La_2NiO_{4+\delta}$ using in-situ high temperature neutron powder diffraction. Solid State Sci., 5 (2003) 419-426.
3. D.J. Buttrey, J.D. Sullivan, G. Shirane, K. Yamada, Influence of oxygen nonstoichiometry on structure and magnetism in $Pr_2NiO_{4+\delta}$. Phys. Rev. B, 42 (1990) 3944-3951.
4. P.M. Geffroy, J. Fouletier, N. Richet, T. Chartier, Rational selection of MIEC materials in energy production processes, Chem. Engn Sci. 87 (2013) 408-413.
5. Y. Zheng, W. Zhou, R. Ran, ZP. Shao, Perovskite as anode materials for solid oxide fuels cells, Progr. Chem. 20 (2008) 413-421.
6. J. Sunarso, S. Baumann, J.M. Serra, W.A. Meulenberg, S. Liu, Y.S. Lin, J.C.D. da Costa, Mixed ionic-electronic conductivity (MIEC) ceramic-based membranes for oxygen separation, J. Membrane Sci. 320 (2008) 13-41.
7. B. Sala, F. Grasset, O. Lacroix, A. Sirat, K. Rahmouni, M. Keddam, H. Takenouti, D. Goeuriot, B. Bendjeriou, Ph. Colomban, A. van der Lee, J.G. Sanchez, Procédé de génération d'hydrogène et d'oxygène par électrolyse de vapeur d'eau, WO 2013053858 A1 (18/04/2013).
8. M. Greenblatt, Ruddlesden-Popper $Ln_{n+1}Ni_nO_{3n+1}$, nickelates: structure and properties. Solid state & Materials Science, 2 (1997) 174-183.
9. G.W. Coors, Protonic ceramic steam-permeable membranes, Solid State Ionics, 178 (2007) 481-485.
10. T. Sakai, K. Isa, M. Matsuka, T. Kozai, Y. Okuyama, T. Ishihara, H. Matsumoto, Int. J. Hydrogen Energy 38 (2013) 6842-6847.
11. J. Daily, S. Fourcade, A. Largeteau, F. Mauvy, J.C. Grenier, M. Marrony, Perovskite and A_2MO_4-type oxides as new cathode materials for protonic solid oxide fuel cells. Electrochimica Acta, 55 (2010) 5847-5853.
12. E. Boehm, Doctorat Thesis, Bordeaux University (2002).
13. A. Slodczyk, Ph. Colomban, Probing the Nanodomain Origin and Phase Transition Mechanisms in (Un)Poled PMN-PT Single Crystals and Textured Ceramics, Materials 3 (2010) 5007-5029.
14. C. Allançon, A. Gonthier-Vassal, J.M. Bascat, J.P. Loup, P. Odier, Influence of oxygen on structural transitions in $Pr_2NiO_{4+\delta}$. Solid State Ionics, 74 (1994) 239-248.
15. M. Zaghrioui, F. Giovannelli, N.Poirot D. Brouri, I. Laffez, Anomalies in magnetic susceptibility of nonstoichiometric $Nd_2NiO_{4+\delta}$ (δ=0.049, 0.065, 0.077, 0.234). Solid State Chem., 177 (2004) 3351-3358.
16. K. Shikawa, K. Metoki, H. Miyamoto, Orthorhombic–orthorhombic phase transitionsion $Nd_2NiO_{4+\delta}$ (0.067< δ <0.224). Solid State Chem., 182 (2009) 2096-2103.
17. E. Boehm, J.-M. Bassat, P. Dordor, F. Mauvy, J.-C. Grenier, Ph. Stevens, Oxygen diffusion andtransport properties in non-stoichiometric $Ln_{2-x}NiO_{4+\delta}$ oxides. Solid State Ionics, 176 (2005) 2717–2725.
18. T. Nakamura, K. Yashiro, K. Sato, J. Mizusaki, Oxygen nonstoichiometry and defect equilibrium in $La_{2-x}Sr_xNiO_{4+\delta}$. Solid State Ionics, 180 (2009) 368-376.
19. T. Nakamura, K. Yashiro, K. Sato, J. Mizusaki, Thermally-induced and chemically-induced structural changes in layered perovskite-type oxides $Nd_{2-x}Sr_xNiO_{4+\delta}$ (x=0, 0.2, 0.4). Solid State Ionics, 181 (2010) 402-411.
20. A. L. Soldati, L. Baqué, F. Napolitano, A. Serquis, Cobalt–iron Red–oxbehavior in Nanostructured $La_{0.4}Sr_{0.6}Co_{0.8}Fe_{0.2}O_{3-\delta}$ Cathodes. Solid State Chem., 198 (2013) 253-261.
21. Ph. Colomban, O. Zaafrani, A. Slodczyk, Proton content and nature in perovskite ceramic membranes for medium temperature fuel cells and electrolysers. Membranes, 2 (2012) 493-509.
22. M.C. Caggiani, Ph. Colomban, Raman identification of strongly absorbing phases: the ceramic black pigments, J. Raman Spectrosc. 42 (2011) 839-843.
23. G. Gouadec, Ph. Colomban, N.P. Bansal, Raman study of Hi-Nicalon-fiber-reinforced Celsian composites: II, Residual stress in Fibers, J. Am. Ceram. Soc. 84 (2001) 1136-1142.
24. A. Slodczyk, O. Zaafrani, M.D. Sharp, J.A. Kilner, B. Dabrowski, O. Lacroix, Ph. Colomban, Testing the chemical/structural stability of proton conducting perovskite ceramic membranes by in situ/ex situ autoclave Raman microscopy. Membranes, 3 (2013) 311-330.
25. S. Upasen, P. Batocchi, A. Slodczyk, Ph. Colomban, F. Mauvy, Structural stability of Ln_2NiO_{4+} ceramics under high temperature and high water pressure operating conditions, Proc. IDHEA 2014 International Discussion on Hydrogen Energy and Applications, Nantes, 12-15 Mai 2014.

26. Ph. Colomban, Proton Conductors-Solids- Membranes and Gels-Materials and Devices. Cambridge University Press, Cambridge, 3rd Edition (2011). DOI: 10.2277/ 052138317X.

27. Ph. Colomban, J. Tomkinson, Novel forms of Hydrogen in solids: the 'ionic' proton and the 'quasi-free proton', Solid State Ionics 97 (1997) 123-134.

28 K.D. Kreuer, Proton-conducting oxides. Ann. Rev. Mater. Res, 33. (2003) 333-359.

29. Ph. Colomban, Latest developments in proton conductors, Ann. Chim. Sci. Mat. 24 (1999) 1-18.

30. Ph. Colomban, C. Tran, O. Zaafrani, A. Slodczyk, Aqua oxyhydroxycarbonate second phases at the surface of Ba/Sr-based proton conducting perovskites: a source of confusion in the understanding of proton conduction. J. Raman Spectrosc., 44 (2013) 312-320.

31. E. Boehm, J.M. Bassat, M.C. Steil, P. Dordor, F. Mauvy, J.C. Grenier, Oxygen transport properties of La2Ni1-xCuxO4+delta mixed conducting oxides, Solid State Sci., 5 (2003) 973-981.

32 A.Slodczyk, Ph. Colomban, G. André, O. Zaafrani, F. Grasset, O. Lacroix, B. Sala, Structural modifications induced by free proton in proton conducting perovskite ceramic membrane. Solid State Ionics 225 (2012) 214-218

33. A. Slodczyk, Ph. Colomban, S. Willemin, O. Lacroix, B. Sala, Indirect Raman identification of the proton insertion in the high temperature [Ba/Sr][Zr/Ti]O_3 modified perovskite protonic conductors. J. Raman Spectrosc. 40 (2009) 513-521.

34. N. Ogita, M. Udagawa, K. Kojima, K. Ohbayashi, Infrared and Raman Study of $(La_{1-x}Sr_x)_2NiO_4$ and $La_2(Ni_{1-x}Cu_x)O_4$. Journal of the Physical Society of Japan, 57 (1988) 3932–3940.

35. M. Udagawa, T. Yamaguchi, N. Ogita, K. Ohbayashi, M. Kato, Y. Maeno, T. Fujita, Raman scattering study of $(La_{1-x}Sr_x)_2NiO_4$. Physica C, 185-189 (1991) 1039-1040.

36. C. Prieto, A. de Andrés, M. Medarde, J.L. Martinez, M.T. Fernandez-Diaz, J. Rodriguez-Carvajal, R. Saez-Puche, F. Fernandez, EXAFS and Raman study of stoichiometric and oxidiez $Nd_2NiO_{4+\delta}$. J. Solid State Comm., 80 (1991) 975-980.

37. W. Wang, Y. Liu, C. Xu, C. Zheng, G. Wang, Synthesis of NiO nanorods by a novel simple precursor thermal decomposition approach. Chem. Phys. Lett, 362 (2002) 119-122.

38. R.E. Dietz, G.I. Parisot, A. E. Meixner, Infrared absorption and Raman scattering by two-magnon processses in NiO. Phys. Rev. B, 4 (1971) 2302-2310.

39. R Laiho, K.G. Lisunov, E. Lähderanta, V.S. Stamov, V.S. Zakhalinski , Ph. Colomban, P.A. Petrenko, Yu.P. Stepanov, Lattice distorsions, magnetoresistance and hopping conductivity in $LaMnO_{3+\delta}$, J. Phys.: Condens. Matter. 17 (2005) 105-118.

40. I.A. Leonidov, M.V. Patrakaeev, J.A. Bahteeva, E.B. Mitberg, V.L. Kozhevnikov, Ph. Colomban, K.R. Pöppelmeier, High-temperature phase equilibria in the oxide systems $SrFe_{1-x}Ga_xO_{2.5}$ - $SrFe_{1-x}Ga_xO_3$ (x = 0, 0.1, 0.2), J. Solid State Chem. 179 (2006) 1093-1099.

41. A. Ubaldini, M.M. Carnasciali, Raman characterisation of powder RE_2O_3 (RE = Nd, Gd, Tm, and Lu), Sc_2O_3 and Y_2O_3. J. Alloys Comp., 454 (2008) 373-378.

42. D. Vijayalakshmi, N.V. Chandra Sekar, S. Ramya, P. Ch. Sahu, G. Meenakshi, Investigation of diphasic region in the Pr_2O_3 + Sm_2O_3 mixed oxide system at various temperatures. J. Alloys Comp., 505 (2010) 733-738.

43. A. Orera, G. Larraz, M.L. Sanjuan, Spectroscopic study of the competition between dehydration and carbonation effects in La_2O_3-based materials. J. Europ. Cer. Soc., 33 (2013) 2103-2110.

44. B.M. Faroldi, J.F. Múnera, L.M. Cornaglia, In situ characterization of phase transformation and reactivity of high surface area lanthanum-based Ru catalysts for the combined reforming of methane. Applied Catalysis B: Environmental, 150-150 (2014) 126-137

45. J. Gouteron, D. Michel, A.M. Lejus, J. Zarembowitch, Raman Spectra of Lanthanide Sesquioxide Single Crystals: Correlation between A and B-Type Structures. J. Solid State Chem., 38 (1981) 288-296.

46. S. Gunasekaran, G. Anbalgan, S. Pandi, Raman and Infrared spectra of carbonates of calcite structure. J. Raman Spectrosc., 37 (2006) 892-899.

47. K. Ohta, R. Iwamoto, Experimental Proof of the Relation Between Thickness of the Probed Surface Layer and Absorbance in FT-IR/ATR Spectroscopy, Appl. Spectrosc. 39 (1985) 418-425.

48. Bruker Application Note, http://www.bruker.com/fileadmin/user_upload/8-PDF-Docs/OpticalSpectrospcopy/FT-IR/ALPHA/AN/AN79_ATR-Basics_EN.pdf (June 2014).
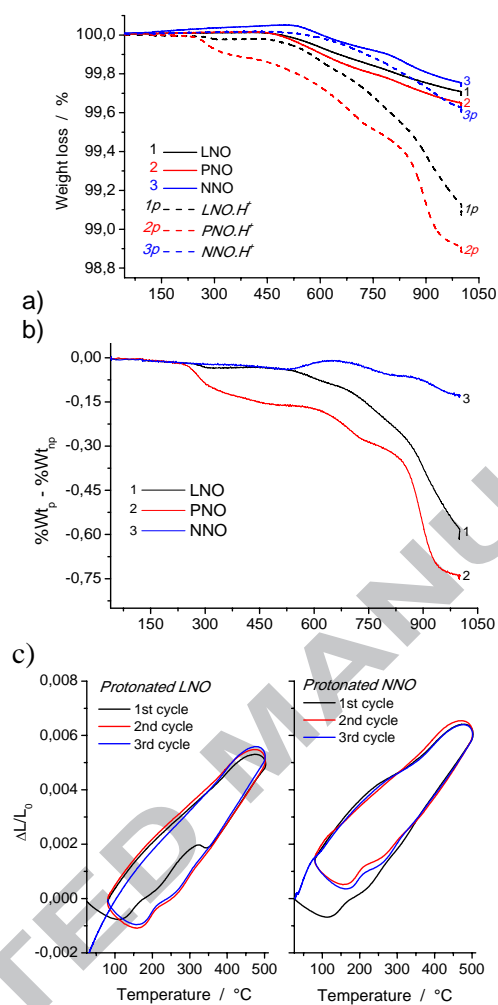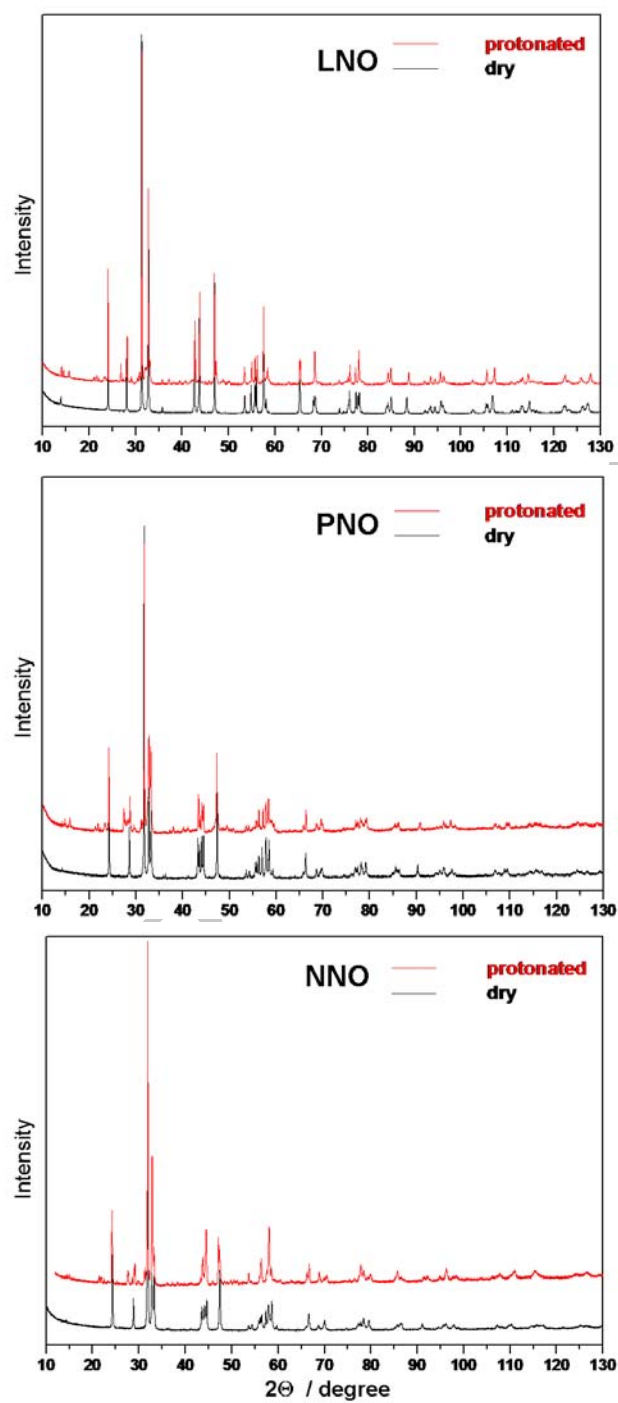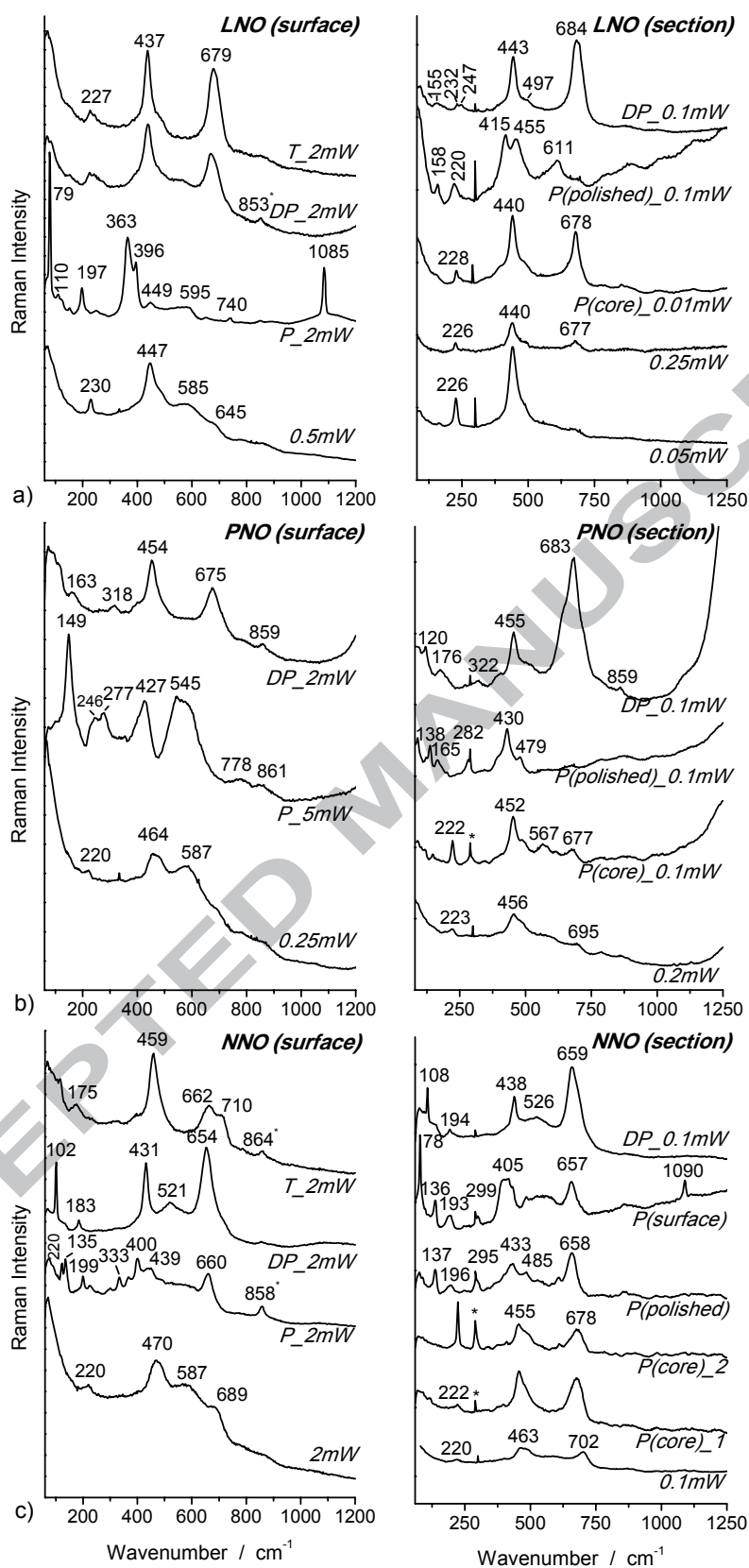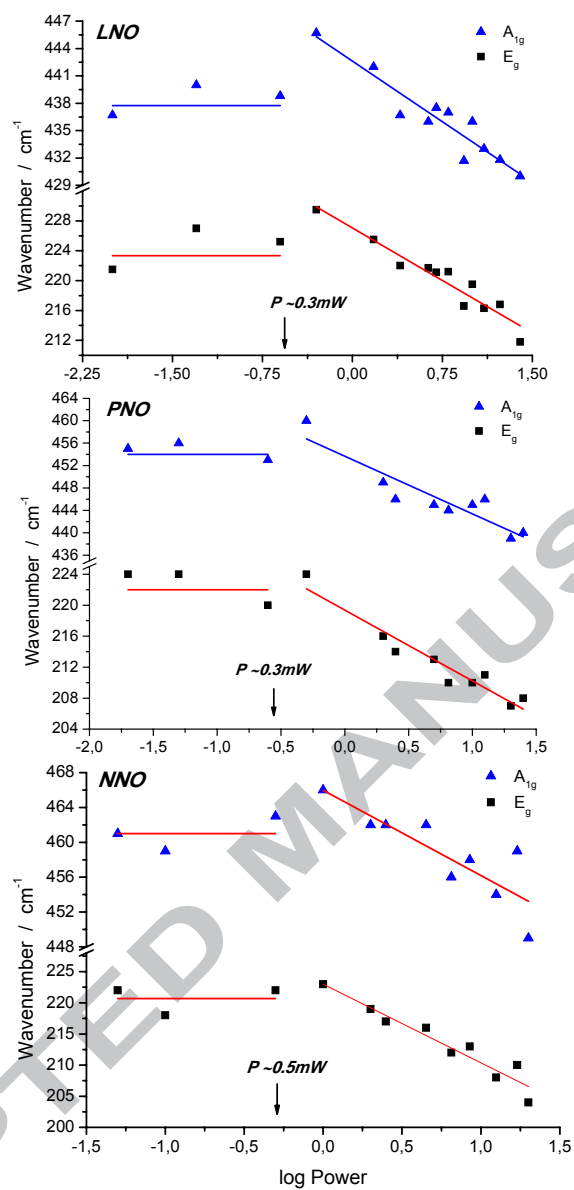
14

a)

b)

c)

Fig. 2

Fig. 3

16

Fig. 4

17

Fig. 5

Fig. 6

Fig. 7

ACCEPTED MANUSCRIPT

Fig. 8

Fig. 9

22
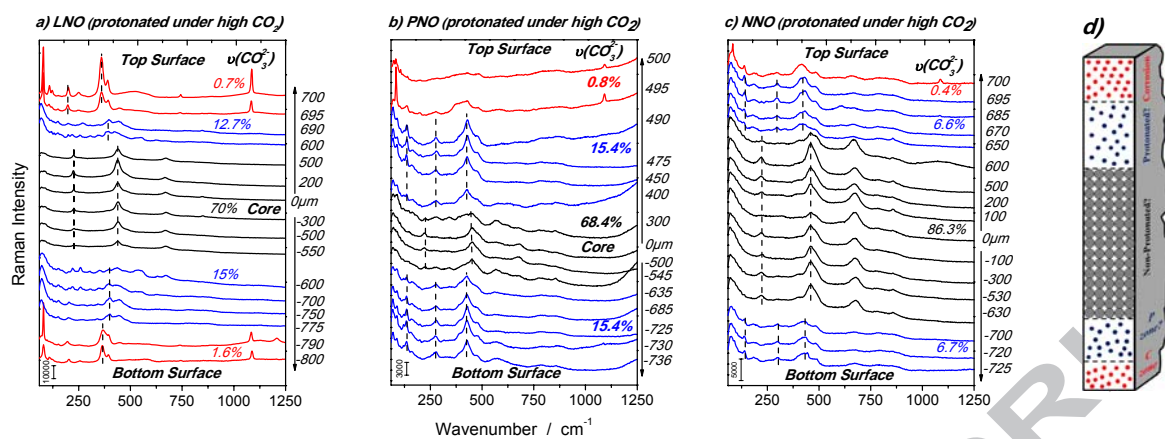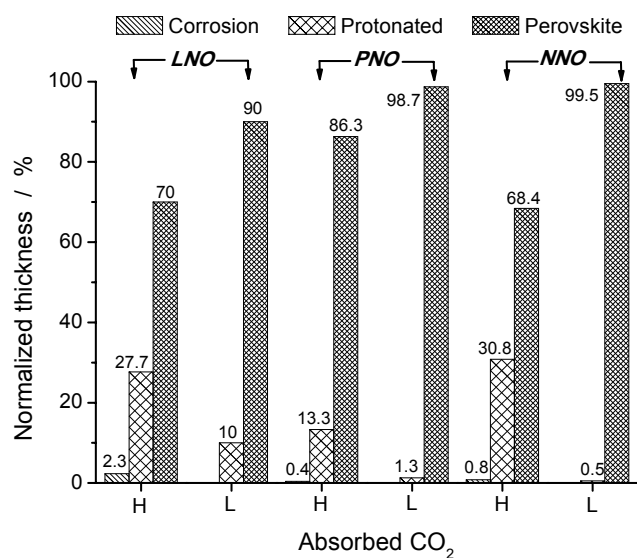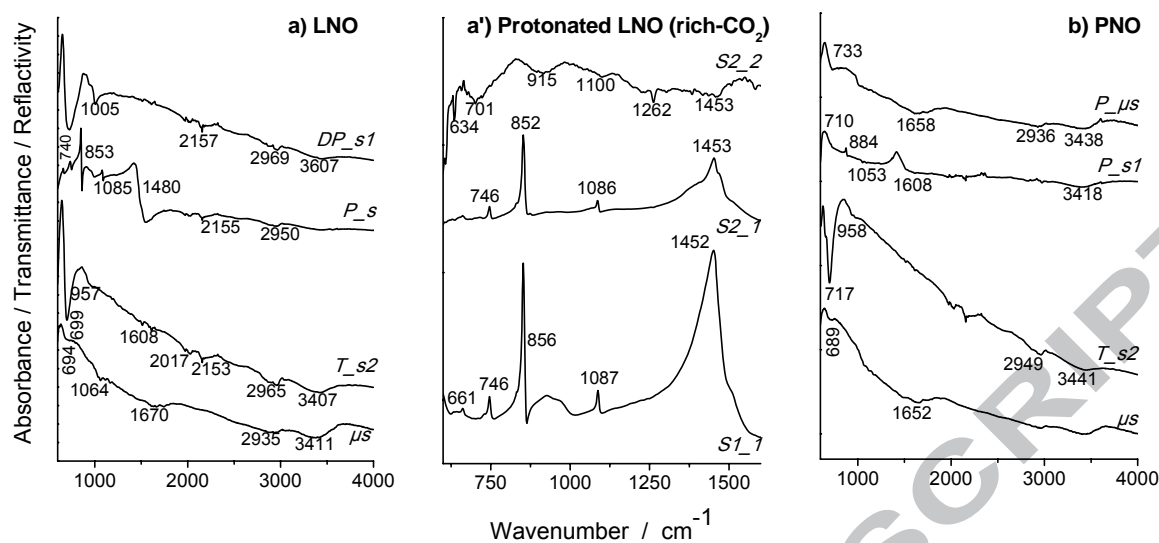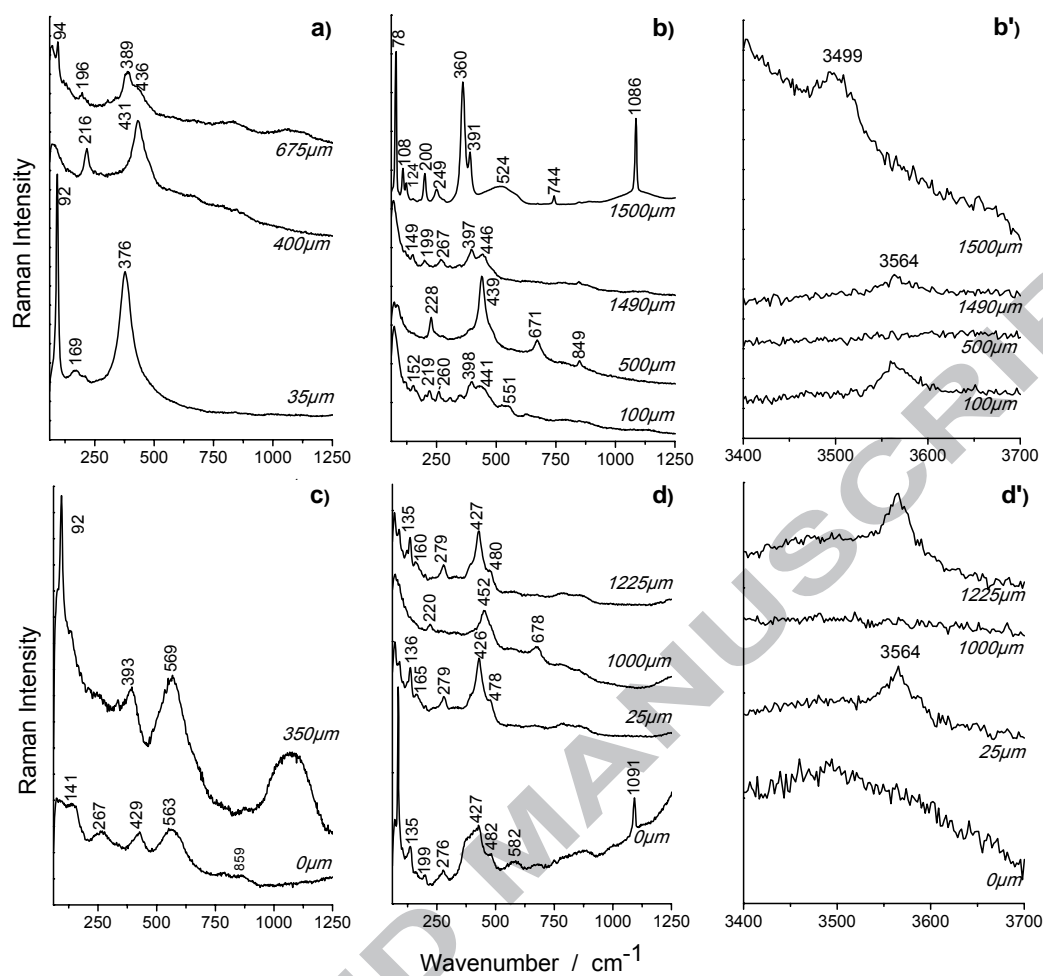
Phase	Symmetry	Unit-cell parameter			Volume	Δ
		a (Å)	b (Å)	c (Å)	V (Å^3)	Δ %
La$_2$NiO$_{4+\delta}$ LNO	Fmmm orthorhombic	5.4682(2)	5.4590(2)	12.6917(4)	378.85(2)	
H-LNO	Fmmm orthorhombic	5.4744(3)-	5.4680(3)	12.6361(5)	378.25(3)	-0.2
	I4/mmm tetragonal	3.689(1)	3.689(1)	12.630(3)	171.86(8)	-9.3
Pr$_2$NiO$_{4+\delta}$ PNO	Bmab orthorhombic	5.3841(2)	5.4646(2)	12.4655(3)	366.76(2)	
H-PNO	Bmab orthorhombic	5.398(1)	5.466(1)	12.401(2)	365.9(1)	-2.3
Nd$_2$NiO$_{4+\delta}$NNO	Bmab orthorhombic	5.3733(4)	5.4586(4)	12.3797(9)	363.10(4)	
H-NNO	Bmab orthorhombic	5.3864(9)	5.4510(8)	12.398(2)	364.02(9)	+2.5
	I4/mmm tetragonal	3.8544(2)	3.8544(2)	12.249(1)	181,98(2)	+0.2

Table 1: Symmetry groups and unit cell parameters of pristine and protonated LnNO ceramics (error in bracket); the pellets have been exposed to lean-CO_2 water.

2nd Phase	La$_2$NiO$_{4+\delta}$ - LNO	Pr$_2$NiO$_{4+\delta}$ - PNO	Nd$_2$NiO$_{4+\delta}$ - NNO
Ln(OH)$_3$	3	10	-
LnOOH	-	13	9
LnH$_2$	-	traces?	-
Ln$_2$O$_3$	4	10	-
Ln$_2$O$_2$CO$_3$	2	-	-
Ln$_4$Ni$_3$O$_{10}$	6	-	-
LnNiO$_3$	-	traces	-
NiO	-	traces	7

Table 2: Relative amount in percent of the phases formed at the surface of LnNO ceramics after treatment in autoclave (550°C, 40 bar, 5 days).

Phase	Symmetry	Main Raman peaks / cm^{-1}			
La$_2$NiO$_{4+\delta}$ LNO	Fmmm Orthorhombic (D$_{2h}$)		224 m	438 S	
core-LNO	Fmmm Orthorhombic (D$_{2h}$)	-	228 w	440 S	678 S
H-LNO	I4/mmm Tetragonal (D$_{4h}$)	158 w	220 w	415,455 S	611 m,b
DP-LNO		155 vw	232,247 vw	443 S, 497sh	684 vS
Pr$_2$NiO$_{4+\delta}$ PNO	Bmab Orthorhombic (D$_{2h}$)		223 vw	454 S	695 vw
core-PNO	Bmab Orthorhombic (D$_{2h}$)		222 w	452 s	677 w,b
H-PNO		165 vw	252 w	430 S 479 sh?	
DP-LNO		176 vw	320 vw	455 m	683 S
Nd$_2$NiO$_{4+\delta}$NNO	Bmab Orthorhombic (D$_{2h}$)		220 w	461 S,b	702 S,b
core-NNO	Bmab Orthorhombic (D$_{2h}$)		222 w	455 S	678 S
H-NNO	I4/mmm Tetragonal (D$_{4h}$)		195 w	433 S	658 S
DP-NNO			183 w	438 m	659 S
La$_{1-x}$Sr$_x$NiO$_4$ [36]			240	450	
Nd$_2$NiO$_4$ [38,39]				440-470	670
Rb$_2$NiO$_4$ [35]		120/188	(358)	405-430	

Table 3: Characteristic peak wavenumber of the LnNO materials in their pristine (LNO, PNO & NNO), protonated (H-LNO, H-PNO & H-NNO) and deprotonated (DP-LNO, DP-PNO & DP-NNO) state. Symmetries deduced from XRD and Raman spectrum are given.

Compound	Main 2nd phase peaks (cm^{-1})
$La_2NiO_{4+\delta}$ - LNO	La_2O_3 :104,<u>197</u>, <u>404</u>
	$La(OH)_3$: <u>138</u>,282,340,<u>450</u>
	LaOOH: <u>123,135,199</u>,312,344,383,424
	I (tetra) $La_2O_2CO_3$: 1064
	Ia (mono) $La_2O_2CO_3$: 1051,1060
	II (hexa) $La_2O_2CO_3$: <u>82,204,364,394,1088</u>
	NiO: 546,<u>1092</u>
$Pr_2NiO_{4+\delta}$ - PNO	Pr_2O_3: 104,187,406,840
$Nd_2NiO_{4+\delta}$ - NNO	Nd_2O_3: 106,<u>191,335,428</u>

Table 4: Main Raman peaks of potential 2nd phase; observed peaks are underlined [44-47].

Normalized in-depth transformation (µm)	$La_2NiO_{4+\delta}$ – LNO		$Pr_2NiO_{4+\delta}$ – PNO	
	Low - CO_2	high water	Low - CO_2	high water
Top layer	-	0.5	0.5	1
Intermediate layer	6	12	-	7
core	90	81	99.5	85
Intermediate layer	4	6	-	7
Bottom layer	-	0.5	-	-

Table 5: Comparison of the in-depth penetration of corrosion and protonation in LnNO dense ceramics.